Available online at www.sciencedirect.com
SCIENCE DIRECT®
Estuarine, Coastal and Shelf Science 60 (2004) 213–228
ESTUARINE COASTAL AND SHELF SCIENCE
www.elsevier.com/locate/ECSS

Floodtide pulses after low tides in shallow subembayments adjacent to deep channels

John C. Warner[a,b,*], David H. Schoellhamer[b], Catherine A. Ruhl[b], Jon R. Burau[b]

[a]U.S. Geological Survey, Coastal and Marine Geology Team, 384 Woods Hole Road, Woods Hole, MA 02543-1598, USA
[b]U.S. Geological Survey, Placer Hall, 6000 J Street, Sacramento, CA 95819, USA

Received 29 July 2003; accepted 26 December 2003

Abstract

In shallow waters surface gravity waves (tides) propagate with a speed proportional to the square root of water depth ($c = \sqrt{g(h+\eta)}$). As the ratio of free surface displacement to mean depth (η/h) approaches unity the wave will travel noticeably faster at high tide than at low tide, creating asymmetries in the tidal form. This physical process is explained analytically by the increased significance of friction and the nonlinear terms in the continuity and momentum equations. In a tidal system comprising a shallow bay adjacent to a deeper channel, tidal asymmetries will be more prevalent in the shallow bay. Thus strong barotropic gradients can be generated between the two, producing rapid accelerations of currents into the bay (relative to other bay tidal processes) and create a maximum peak in the flood tide that we describe as a floodtide pulse. These floodtide pulses can promote a landward flux of suspended-sediment into the bay.

In Grizzly Bay (part of northern San Francisco Bay, USA), field observations verify the occurrence of floodtide pulses during the lowest low tides of the year. No pulses were observed in neighboring Honker Bay, which has an average depth ~30 cm greater than Grizzly Bay. Numerical simulations of northern San Francisco Bay using realistic bathymetry demonstrated that floodtide pulses occurred in Grizzly Bay but not in Honker Bay, consistent with the observations. Both observations and numerical simulations show that floodtide pulses promote a landward flux of sediment into Grizzly Bay. Numerical simulations of an idealized bay–channel system quantify the importance of mean depth and friction in creating these floodtide pulses.

Keywords: floodtide pulse; sediment transport; San Francisco Bay, CA, USA

1. Introduction

Shallow estuarine waters are important for biological productivity, they provide habitat for migratory and indigenous fish and bird species, they act as filters for sediment and pollutants that drain from watersheds, absorb wave energy to reduce impacts from storms, and provide cultural and recreational benefits. Shallow estuarine waters are ecologically significant as they provide areas for shelter and nourishment for a large fraction of the biota in estuarine systems.

Shallow estuarine waters affect the hydrodynamic propagation of the tide and affect the generation of tidal asymmetries. In shallow water the tide propagates as a gravity wave with speed $c = \sqrt{g(h+\eta)}$ where g is the acceleration of gravity, h is the mean water depth, and η is the free surface displacement measured positive upwards from the mean water level. For the case where a deep channel is adjacent to a shallow bay the wave speed (c) can be several times larger in the channel compared to the bay (Fig. 1). When the relative depth in the bay (h_b) to depth in the channel (h_c) approaches zero, for example in the limiting case of a tidal mud flat that becomes dry, the tide would propagate infinitely faster in the channel as compared to the "dry" bay. For the other extreme when the depth in the bay equals the depth in the channel, the tide would propagate at equal rates (Fig. 1). Lateral velocity gradients will tend to smooth the difference in tidal propagation between the bay and channel.

* Corresponding author.
E-mail address: jcwarner@usgs.gov (J.C. Warner).

0272-7714/$ - see front matter © 2004 Elsevier Ltd. All rights reserved.
doi:10.1016/j.ecss.2003.12.011

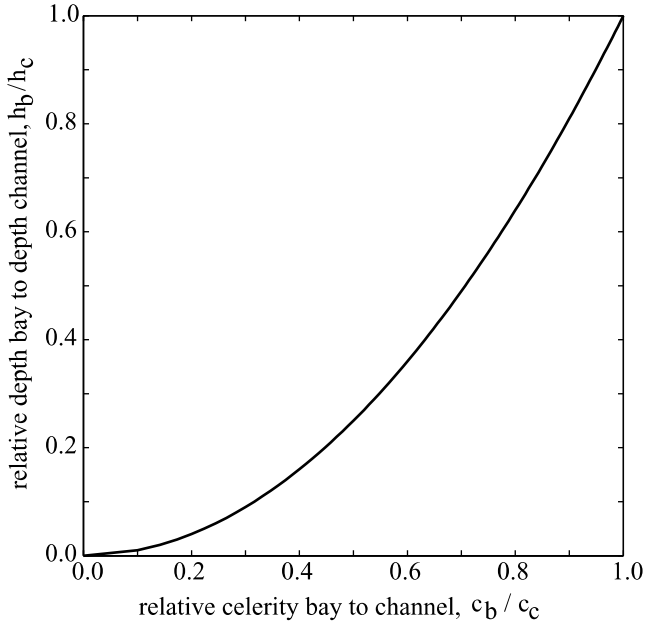

Fig. 1. Relative depth of bay (h_b) to channel (h_c) vs. relative phase speed in bay (c_b) to channel (c_c).

In a shallow bay the ratio of tidal displacement to mean depth may be of order one ($\eta/h \sim O(1)$) allowing the propagation speed of the tide to be measurably faster during high tide than low tide. The resulting wave will be distorted from the original sinusoidal shape with high tide occurring earlier and low tide later. Subtraction of the distorted tide from the original shape reveals the development of overtides (higher harmonics of astronomical tides) and compound tides (astronomical tidal interaction) (Aubrey and Speer, 1985; Speer and Aubrey, 1985; Friedrichs et al., 1992). Parker (1991) described the generation of tidal asymmetries by analyzing the terms in the shallow water equations, which in two dimensions are:

$$\frac{\partial \eta}{\partial t} + \frac{\partial(\bar{u}(h+\eta))}{\partial x} + \frac{\partial(\bar{v}(h+\eta))}{\partial y} = 0 \tag{1}$$

$$\frac{\partial \bar{u}}{\partial t} + \bar{u}\frac{\partial \bar{u}}{\partial x} + \bar{v}\frac{\partial \bar{u}}{\partial y} = -g\frac{\partial \eta}{\partial x} - C_d\frac{\bar{u}|V|}{h+\eta} \tag{2}$$

$$\frac{\partial \bar{v}}{\partial t} + \bar{u}\frac{\partial \bar{v}}{\partial x} + \bar{v}\frac{\partial \bar{v}}{\partial y} = -g\frac{\partial \eta}{\partial y} - C_d\frac{\bar{v}|V|}{h+\eta} \tag{3}$$

where $\bar{u}(x,y,t)$ and $\bar{v}(x,y,t)$ are the depth-integrated along channel (x-direction) and lateral (y-direction) velocities, $|V(x,y,t)|$ is the magnitude of total velocity, t is time, $\eta(x,t)$ is the water surface displacement measured positive upwards from the mean water level $h(x,y)$, g is the acceleration due to gravity, and C_d is a friction coefficient (typically value 0.0025). There are six nonlinear terms in these equations that generate tidal asymmetries. (1) The nonlinear continuity term $\partial(\bar{u}\eta)/\partial x$ (likewise $\partial(\bar{v}\eta)/\partial y$) produces the asymmetric effect equivalent to a faster wave celerity at high tide and slower celerity at low tide. (2) The convective acceleration term $\bar{u}\,\partial\bar{u}/\partial x$ (likewise $\bar{v}\,\partial\bar{v}/\partial y$) provides asymmetry by enhancing the wave celerity ($c+u$) at high tide and decreasing wave celerity at low tide ($c-u$). (3) The friction term $C_d\bar{u}|V|/(h+\eta)$ (likewise $C_d\bar{v}|V|/(h+\eta)$) actually contains two nonlinear aspects—the quadratic velocity part and the effect of η in the denominator. First order effects of friction are to decrease wave celerity and decrease the wave amplitude—thus high and low tide will be delayed. Nonlinear effects from the friction term due to η in the denominator provide less frictional loss of momentum at higher tide and greater frictional loss at low tide, creating an asymmetry that generates M4 and other even harmonics (Parker, 1991).

For a given tide that forces a bay–channel configuration, more tidal asymmetries will develop in the shallow bay due to the increased importance of friction and larger η/h ratio than in the channel. Thus the free surface in the bay will be different than in the channel and barotropic gradients (pressure gradients due to differences in free surface elevation) will develop between the bay and the channel, producing rapid accelerations of currents into the bay (relative to other bay tidal processes) and create a maximum peak in the flood tide that we describe as a floodtide pulse.

Previous research discussing bay to channel exchanges and interactions are limited. Schuepfer et al. (1995) discuss sea level gradients that develop across the mouth of tributaries. These gradients are in the direction of tidal propagation in the main channel, but are in the lateral (cross channel) direction in the tributary mouth, thus producing a rotary current structure. Valle-Levinson and O'Donnell (1996) and Li and O'Donnell (1997) discuss tidally driven residual circulation in shallow estuaries with lateral depth variations. In these studies the channel depth varied laterally (as opposed to a separate defined bay structure that we discuss). Results identified larger inward flux in the shallower regions due to higher tidal nonlinearities at shallower depths. Other results suggest that lateral pressure gradients were not as important to the overall estuarine circulation. This is due to the geometry of their system. In our paper the lateral gradients will be identified as significant due to the bay only being driven tidally from the channel, not from the estuary mouth.

In this paper we examine a shallow bay–deep channel configuration and explore the generation of floodtide pulses that occur in the shallow bay after low tide. We use field observations and numerical models to investigate floodtide pulses. Data from two shallow subembayments of San Francisco Bay, Grizzly and Honker Bays, are used to explore the essential relations of floodtide pulses. A three-dimensional numerical simulation using realistic bathymetry shows that floodtide pulses occur in Grizzly Bay and are absent in Honker Bay. Finally, pulses are simulated with a numerical model of an

idealized shallow bay adjacent to a deep channel. Of the terms in Eqs. (1)–(3), the mean depth (h) and friction coefficient (C_d) are varied to determine their affects on generation of tidal asymmetries in the free surface (η) and to identify the relative importance to the magnitude of the floodtide pulses.

2. Field observations in Suisun Bay

2.1. Methods

San Francisco Bay (Fig. 2) is divided into four main subembayments: South Bay, Central Bay, San Pablo Bay, and Suisun Bay. The mean depth of San Francisco Bay is 6 m at mean lower low water, however, one-half of its surface area is less than 2 m deep (Conomos et al., 1985). The deeper straits of the Bay are partially mixed and the shallow areas of the sub-basins are often well mixed due to strong tidal current shears and wind induced mixing. The principal source of freshwater inflow to the bay is drainage from the Central Valley of California via the Sacramento and San Joaquin Rivers that merge to form the Sacramento/San Joaquin River Delta, connected to the eastern end of Suisun Bay. Most inflow to the Bay occurs during winter and spring.

Suisun Bay is further subdivided into Grizzly and Honker Bays (Fig. 2). Grizzly Bay covers approximately 24 square kilometers (km^2) and Honker Bay covers approximately 10 km^2. Both subembayments are shallow with most areas being less than 2 m in depth. The average water depth, defined as the volume at mean lower low water divided by the surface area, is 125 cm in Grizzly Bay and 157 cm in Honker Bay. The tides are semi-diurnal with a range of approximately 2 m in this area.

Basin geometry to a great degree influences tidal propagation, tidal and residual circulation and mixing in shallow bays. Major bathymetric features of Grizzly Bay include Garnet Sill located at the mouth and two sloughs that feed into the northwest portion of Grizzly Bay (Fig. 2). The transition from deep to shallow water is relatively rapid in both Grizzly and Honker Bays. For example, the channel that borders Grizzly Bay has a depth of 8 m but shallows to about 4–6 m along the entrance of Grizzly Bay. Channel water enters directly into Grizzly Bay during flood tides while channel water bypasses the bay during ebb tides. The geometry of Honker Bay, on the other hand, is characterized by an extremely shallow bar at the mouth, and Spoonbill Creek, which connects the head of the Bay to Suisun

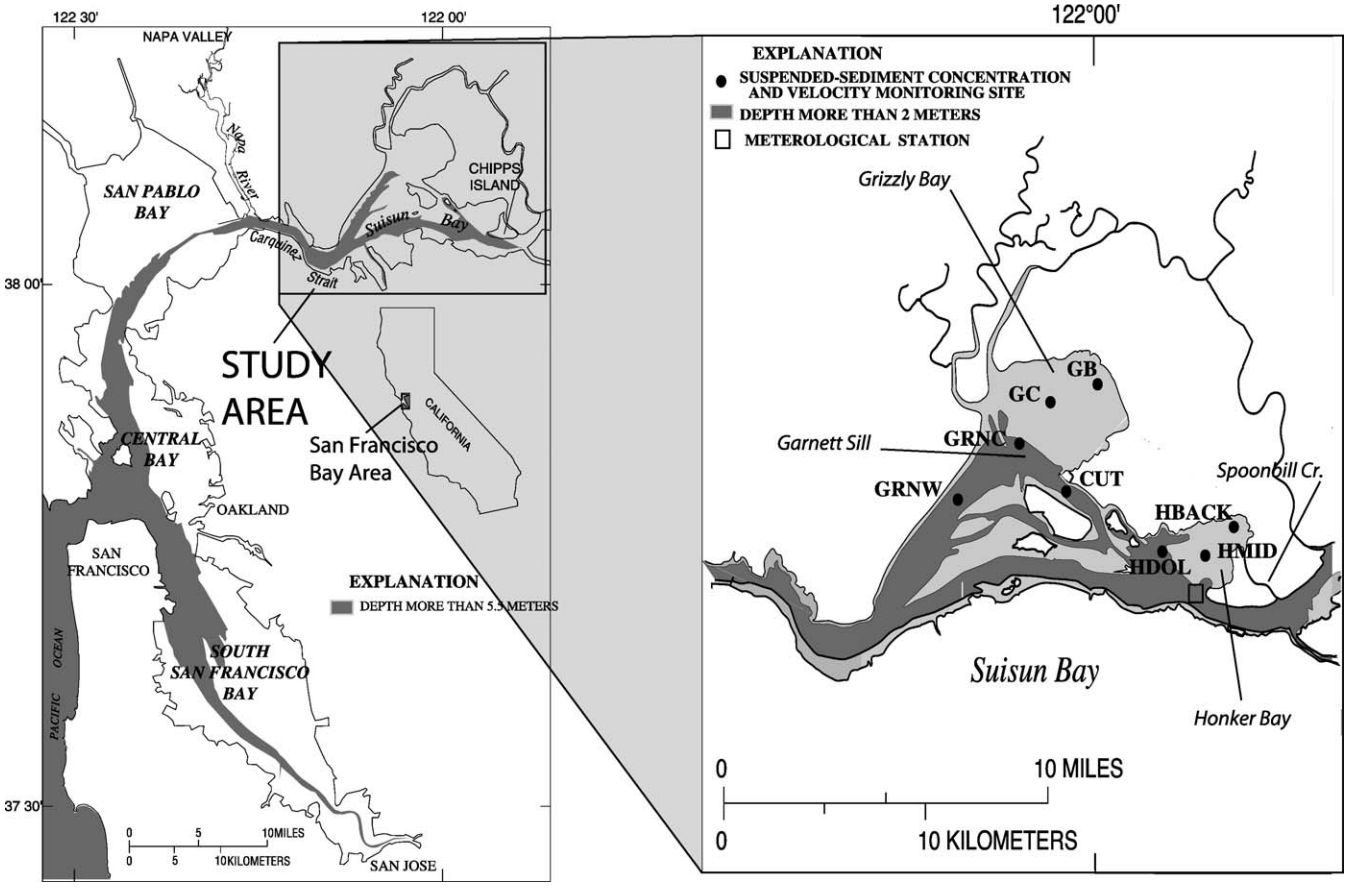

Fig. 2. Bathymetric contours and site map of Suisun Bay showing Grizzly and Honker Bays in Northern San Francisco Bay.

Bay east of Mallard Island (Fig. 2). The flood currents in Honker Bay enter through the western corner and exit at the southern corner of Honker Bay (Lacy, 2000) because of the orientation of the deep channel (6–15 m) adjacent to Honker Bay and the shallow bar at the mouth.

Data presented in this paper were collected in two separate field experiments. The first experiment was conducted in Honker Bay from December 1996 through August 1997 and data from three stations, HBACK, HMID, and HDOL will be presented in this paper. Sites HBACK and HMID (mean depths 1.6 m) are located in the shallow interior parts of Honker Bay and site HDOL (mean depth 7.7 m) is located in the deep entrance channel adjacent to the Bay (Ruhl and Schoellhamer, 1999).

In this paper, we focus primarily on observations of tidal dynamics and suspended-sediment data collected during the second experiment at channel–bay locations in Grizzly Bay from August 1999 through June 2000. Equipment was deployed at sites in the back (GB) and central (GC) parts of the bay, in the main channel at the bay mouth (GRNC), and on opposite sides of the bay (sites GRNW and CUT) as part of a larger study (Fig. 2). Tidal current point velocities were measured at GB (mean depth $\sim$1.6 m) and GC (mean depth $\sim$2.1 m) while vertical velocity profiles were measured using an acoustic Doppler current profiler (ADCP) at GRNC (mean depth $\sim$3.5 m). Site GRNC is located on the northern edge of the channel near Garnett Sill, a local bathymetric rise. The channel is on the order of 8 m in depth, the mean depths at sites GRNW and CUT are $\sim$8.5 m and $\sim$9.5 m, respectively.

Suspended-sediment concentration (SSC) data were collected at all five sites typically at 10-min or 15-min intervals. Biological fouling and instrument difficulties compromised some data at all sites, and ultimately eliminated all SSC data from site GB. SSC data were calculated from a linear regression calibration between logger voltage and water samples obtained during the deployment. Table 1 summarizes the deployment sensor heights and site depths.

2.2. Hydrodynamic results

Data from Grizzly Bay confirm the presence of floodtide pulses at the lowest low tides. In the back of the bay the depths become very shallow at low tide—less than 1 m at most locations, especially at the lower low tides of December 1999 during the observational period. Fig. 3A shows a time series of observed depth variations at site GC, displaying the strong semi-diurnal nature of the tidal signal in December. The lowest low tide occurs at midnight between December 21 and 22. Because of the shallow depths in the bay the generation of tidal asymmetries is greatly increased in Grizzly Bay compared to that in the main channel, which has depths on the order of 8 m. Fig. 3B shows the sea level difference from the front (site GRNC) to the back (site GB) of the bay, calculated as the difference in high frequency water level (measured time series of sea level minus low pass filtered). At the beginning of the flood tide, the water surface elevation at the mouth of Grizzly Bay (GRNC) was as much as 15 cm greater than at the back of Grizzly Bay (GB). These sites are separated by a distance of 2670 m that yields a barotropic gradient ($\partial\eta/\partial x$) on the order of 5×10^{-5} m/m.

Table 1
Deployment site depths and sensor heights

Site	Mean depth (m)	Velocity height (m)	SSC height (m)
GB	1.6	Point, 0.45	–
GC	2.1	Point, 0.45	0.3
GRNC	3.5	Point, 0.45	0.3
GRNW	8.5	Profile	1.0, 6.0
CUT	9.5	Profile	1.0, 6.5
HDOL	7.7	Profile	1.0, 5.0
HBACK	1.6	Point, 0.45	0.3
HMID	1.6	Point, 0.45	0.3

The differences in sea level are most significant at the lower low tides, with the first discernable pulse at lower low tide on December 20. These extreme differences in water level cause large barotropic accelerations toward the back of Grizzly Bay at the beginning of flood tide, greatly increasing current speed at the center of Grizzly Bay (GC). Fig. 3C shows the magnitude of velocity at site GC, positive in the flood direction 60° east of true north. Spikes in the barotropic gradient from the front to the back of Grizzly Bay coincide with pulses in velocity at site GC (in the center of the bay). The pulse on December 21 was greater than the others because a sustained northerly wind event (not shown) created a lower than normal water surface at the northern end of the bay and a larger than normal barotropic gradient resulting in an increased velocity amplitude. The wind event enhanced the magnitude of the floodtide pulse, but was not necessary for its generation.

The difference in sea level from site GRNC to site GB is a function of both astronomical tides and shallow water (nonlinear) tides. A harmonic analysis of the measured free surface at sites GRNC and GB identifies 11 predominant tidal constituents (Table 2 for both sites). Magnitudes of the astronomical tides (O1, K1, N2, M2, L2, and S2) are consistent for both sites, but the magnitudes of the nonlinear tides (MO3, MK3, M4, MS4, and 2MK5) are greater at GB than GRNC. Fig. 4 shows the difference in water level between sites GRNC and GB calculated by three methods. The solid line uses the complete observed time series from both sites (identical to Fig. 3B). The long dashed line (offset 20 cm for clarity) was calculated by using only the astronomical tides in Table 2 to reconstruct the water levels at both sites and then differencing. When compared to the difference using the complete time series, the astronomical tide method provides a correlation coefficient of only

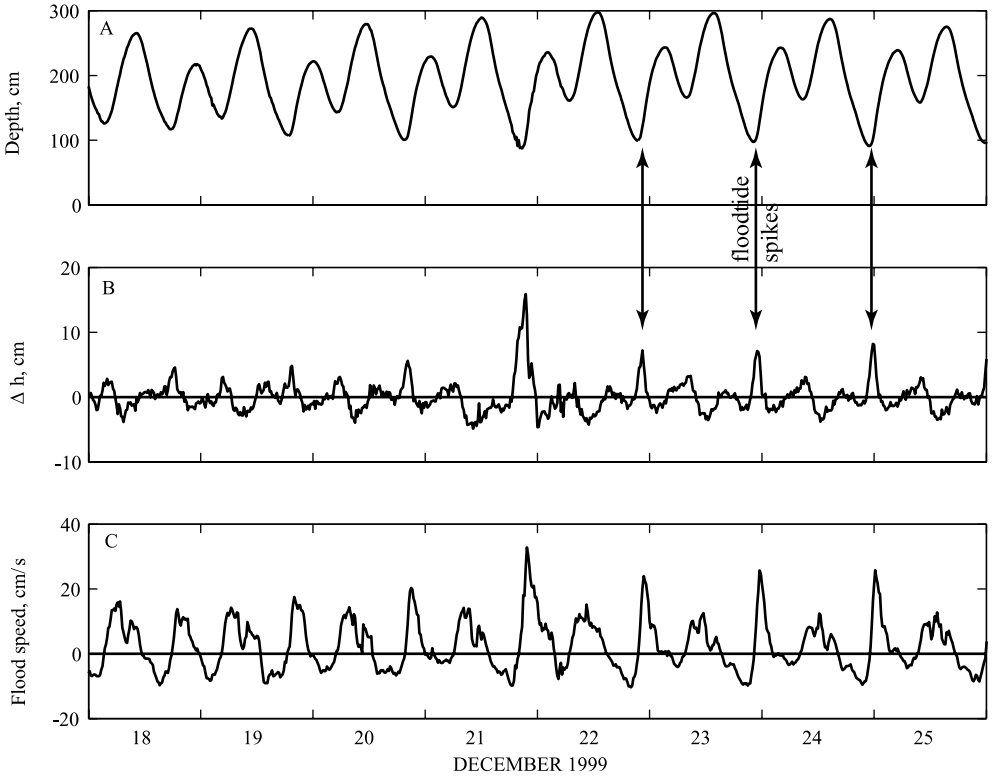

Fig. 3. Floodtide pulses at low tide in Grizzly Bay. Field observations of (A) sea level at site GC in center of bay; (B) high frequency water surface difference from bay mouth at site GRNC to back of bay at site GB; (C) magnitude of velocity at site GC in bay center.

$r^2 = 0.61$ to explain the variance of the water level difference. The short dashed line (offset 10 cm for clarity) was calculated by using both the astronomical and shallow water tides in Table 2 to reconstruct the water levels and then differencing. This method yields an $r^2 = 0.81$ to explain the variance of the water level difference, and captures the main features of the strong gradients that produce the floodtide pulses. Therefore, the nonlinear tides are necessary to produce the strong barotropic gradients and create the floodtide spikes.

Considering the entire period of record at the center of Grizzly Bay, maximum flood speed increases as the depth of low water decreases, especially for depths less than 100 cm (Fig. 5). After low tides less than 100 cm, all subsequent maximum flood speeds were greater than 15 cm/s. After low tides greater than 120 cm, all subsequent maximum flood speeds were less than 20 cm/s. The monotonic trend of maximum flood speed increasing with decreasing depth of low water is statistically significant ($p = 0.001$) according to the Kendall τ and Spearman ρ tests (Conover, 1980; Helsel and Hirsch, 1992). The ratio of maximum flood speed to the mean speed of the adjacent ebbs increases in a similar manner as the depth of low water decreases (not plotted). Thus,

Table 2
Sea level tidal constituents at sites GRNC and GB

Name	Cycles/day	GRNC		GB	
		Amplitude (cm)	Phase (κ')	Amplitude (cm)	Phase (κ')
O1	0.9295	16.24	292.94	16.62	294.17
K1	1.0027	37.04	164.56	37.65	164.71
N2	1.8959	11.19	150.40	11.53	149.99
M2	1.9322	47.82	201.97	49.13	201.87
L2	1.9685	5.35	239.13	5.49	237.89
S2	2.0000	7.71	73.89	7.84	75.10
MO3	2.7106	5.23	65.18	5.93	63.30
MK3	2.9350	4.48	298.55	5.27	294.80
M4	3.8645	1.43	315.13	2.03	315.61
MS4	3.9322	1.51	182.47	1.81	186.65
2MK5	4.8672	2.88	293.92	3.22	299.77

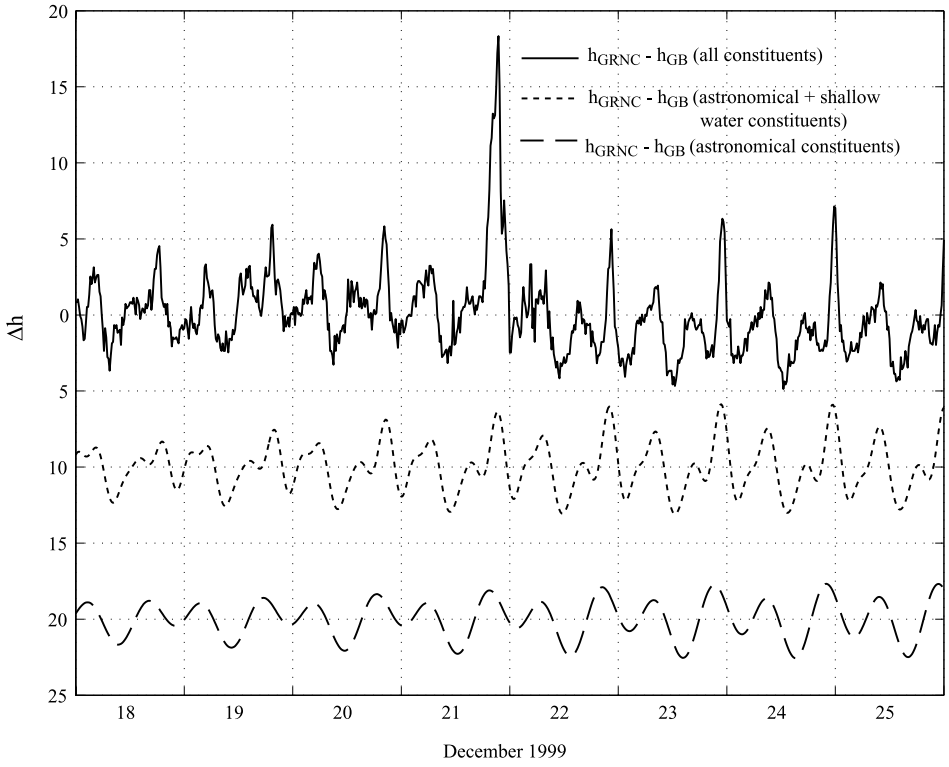

Fig. 4. Difference in sea surface height from bay mouth at site GRNC to back of bay at site GB calculated from full observational data (solid line, same as Fig. 3B), astronomical and shallow water tides from Table 2 (short dashed line), and astronomical tides from Table 2 only (long dashed line).

Grizzly Bay becomes more flood dominant as the depth of low water decreases.

2.3. Suspended-sediment concentrations

Temporal variations in suspended-sediment concentrations (SSC) occur at both tidal and seasonal scales. Tidally, the SSC at site GC typically has two peaks per day during spring months. The suspended-sediment peaks coincide with slack after ebb, are in quadrature with the tidal currents, and thus advection is a critical process in the temporal evolution of SSC variability. The mobilization of the sediment is dependent upon wind stress with peaks in SSC correlating with strong wind speeds (not shown). The spring/neap cycle is important for resuspension in the channels because typically, tidal velocities during spring tides are increased by a factor of $\sim$2 causing greater resuspension. The spring/neap cycle does appear to be less important in shallow embayments where the effect of wind typically plays a crucial role (Ruhl et al., 2001; Ruhl and Schoellhamer, in press). Seasonally the SSC varies with higher concentrations in the spring months and lower concentrations in the fall. During the spring months after the supply of sediment has been transported to SF Bay, the shallow embayments such as Grizzly Bay can act as a source of sediment (Krone, 1979).

Floodtide pulses increase the landward transport of suspended-sediment in Grizzly Bay. As an example, the observed time series of sea level at site GC (Fig. 6A) features very low tides during March 20 and 21, 2000. The difference in water surface elevation between the mouth (GRNC) and back (GB) of Grizzly Bay was 10 cm (Fig. 6B) and the subsequent floodtide pulses at the center of the bay (GC) were greater than 20 cm/s (Fig. 6C). Velocity magnitude is shown with positive flood direction as 60° east of true north. SSC in the center of Grizzly Bay (GC) is greatest at low slack tide because wind–wave resuspension increases as water depth decreases and more turbid water is transported from shallower more turbid waters (Fig. 6D). Floodtide pulses and maximum SSC caused large landward transport of suspended-sediment during the beginning of flood tides. The tidally averaged suspended-sediment flux shifted from seaward to landward during the days with floodtide pulses (Fig. 6E).

2.4. Honker Bay

In Honker Bay no floodtide pulses were observed, probably due to greater water depths or configuration of channel geometry at the bay entrance. Time series of observed water level at sites HDOL and HBACK are shown in Fig. 7A during June of 1997, during a time period of increased tidal range similar to the time periods of Figs. 3 and 6. The free surface displacement

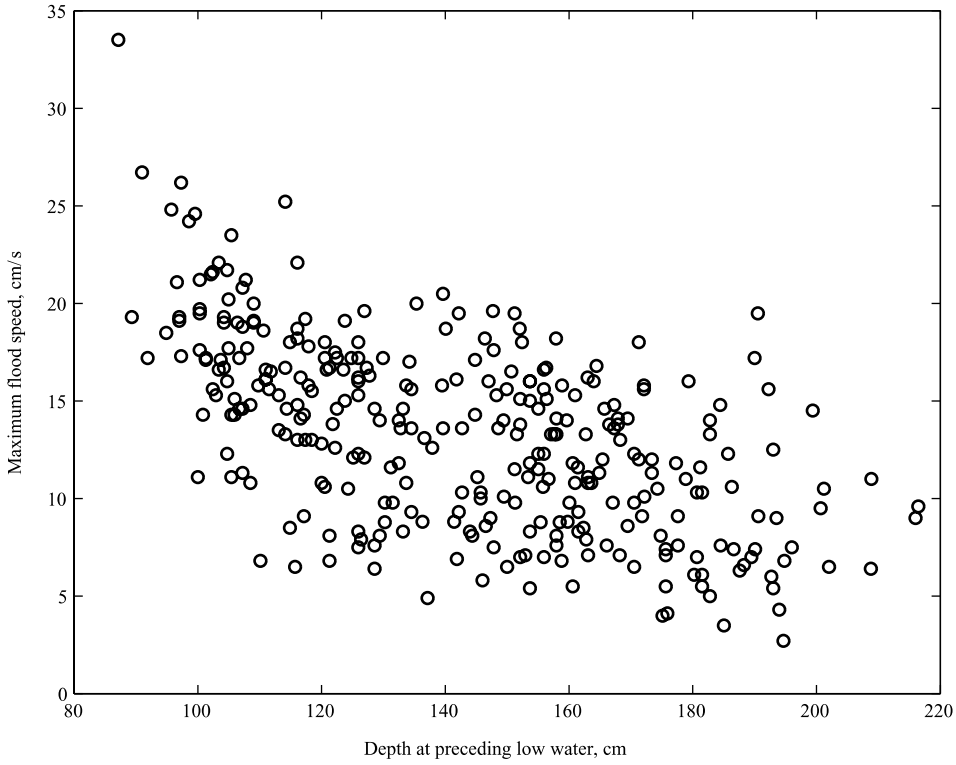

Fig. 5. Maximum flood speed as a function of depth at preceding low water, center of Grizzly Bay (GC).

at HDOL (near the bay entrance) and HBACK (at the back of the bay) is in phase with approximately the same amplitude. The difference of these water levels is shown in Fig. 7B, which does not display a large difference at the lower low waters (as was observed in Grizzly Bay in Fig. 3B). The magnitude of observed flood speed at the center of Honker Bay at site HMID is shown in Fig. 7C, positive in the direction 120° east of true north. There are no discernable spikes in the observed velocity as seen in Grizzly Bay (compare to Fig. 3C).

Data from Grizzly Bay showed that the existence and magnitude of the floodtide pulse is sensitive to water depth (Fig. 5). The average mean lower low water depth in Honker Bay is 32 cm greater than in Grizzly Bay. Assuming that the relation between pulse magnitude and water depth would be the same in Honker Bay as in Grizzly Bay, an increase in water depth of 32 cm would reduce the occurrence of definitive floodtide pulses in Honker Bay.

3. Numerical simulation of Suisun Bay

3.1. Methods

To further investigate the specific dynamics of the floodtide pulse, a numerical model is applied to Suisun Bay using realistic bathymetry. The numerical model is the Regional Ocean Modeling System (ROMS v2.0), a free surface hydrostatic finite difference model with horizontal orthogonal curvilinear grid and stretched terrain following coordinates in the vertical (Chassignet et al., 2000; Haidvogel et al., 2000; Ezer et al., 2002; Shchepetkin and McWilliams, in press). ROMS is a recently developed public domain model with many features such as higher order advection schemes, computational efficiency on both single and multi-threaded computer architectures, and multiple advanced turbulence closures.

Bathymetry was obtained from the UTM projection, 100 m sampled mean sea level data set from http://sfbay.wr.usgs.gov/access/Bathy/grids.html. A horizontal curvilinear grid was constructed to consist of 120×40 cells (Fig. 8) and the vertical dimension was discretized with 10 vertical terrain following (sigma) levels. This grid provided a horizontal resolution on the order of 200 m in the x-direction, 250 m in the y-direction, and between 2.0 and 0.2 m in the vertical. At the western open boundary an oscillatory free surface displacement was prescribed from O1, K1, M2, S2, N2, and M4 harmonic components (Table 3). These represent the principal diurnal, semi-diurnal, and shallow water overtides. At the eastern and northern boundaries a radiation condition is imposed on the depth-averaged velocities to allow the tide to propagate without reflection from the domain. Additionally, the eastern boundary was forced with a depth-averaged riverine velocity of 0.03 m/s. For the simulations presented here, subgrid

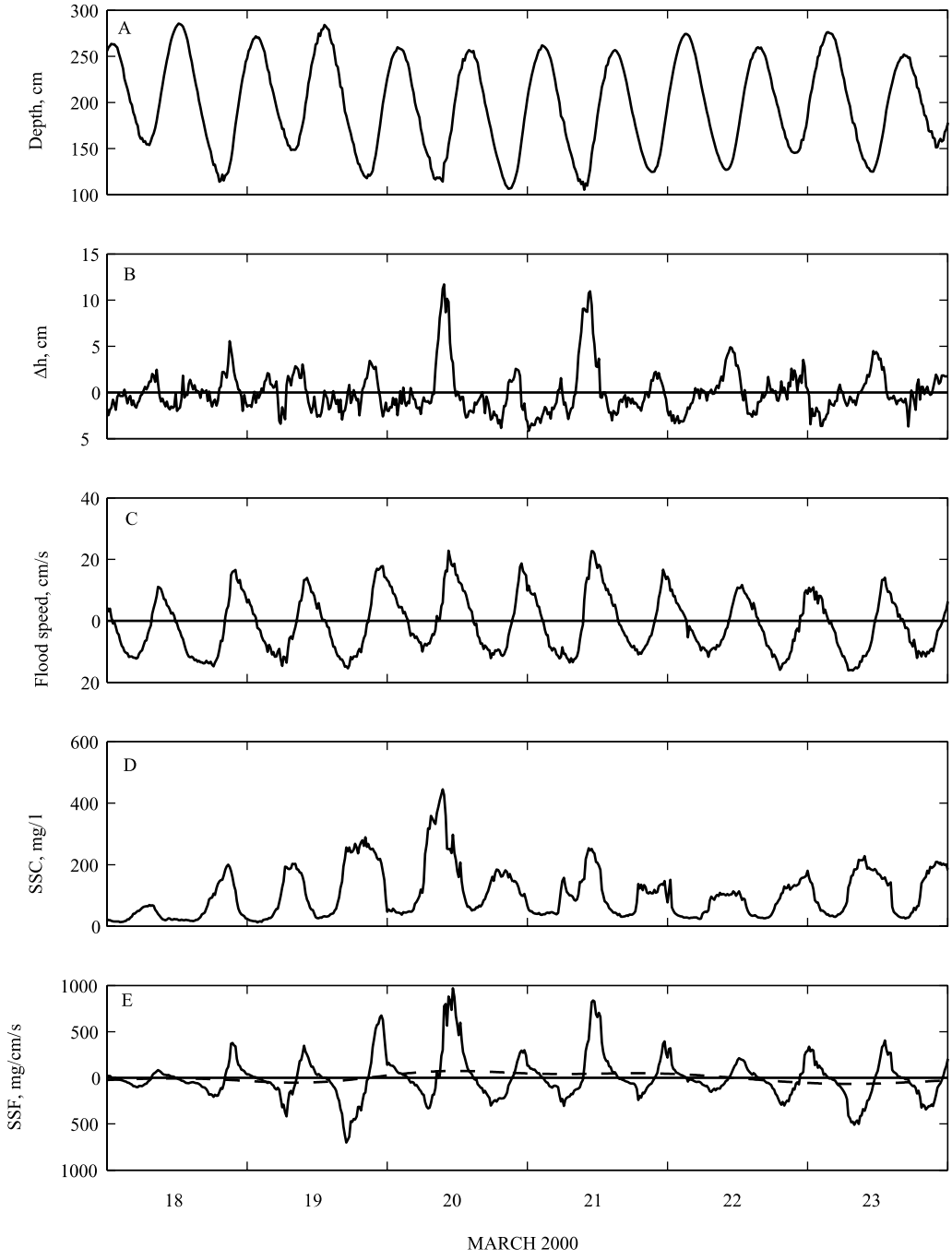

Fig. 6. Effect of floodtide pulses at low tide on suspended-sediment flux in Grizzly Bay. (A) Depth at site GC; (B) high frequency water surface difference between the mouth (GRNC) and back (GB) of Grizzly Bay; (C) flood speed at GC; (D) suspended-sediment concentration at GC; and (E) flood suspended-sediment flux (solid line) and tidally averaged (dashed) at GC.

scale parameterizations for the mixing of momentum and tracers are accomplished with the two-equation turbulence closure $k-\omega$ model (Wilcox, 1988; Umlauf et al., 2003). The implementation of this closure into ROMS is discussed in detail in Warner et al. (in press). Bottom stress is parameterized with a spatially uniform roughness coefficient $C_d = 0.002$.

Suspended-sediment transport is modeled by the solution to the advection–diffusion equation with the added characteristics of a sink term to account for gravitational settling and a source term based on an excess shear erosional flux following Ariathurai and Arulanandan (1978) as:

$$E_s = E_0(1-\varphi)\frac{\tau_b - \tau_{ce}}{\tau_{ce}} \quad \text{when } \tau_b > \tau_{ce} \tag{4}$$

where E_s is the surface erosion mass flux ($\mathrm{kg\,m^{-2}\,s^{-1}}$), E_0 is a bed erodibility constant ($= 1 \times 10^{-4}\ \mathrm{kg\,m^{-2}\,s^{-1}}$),

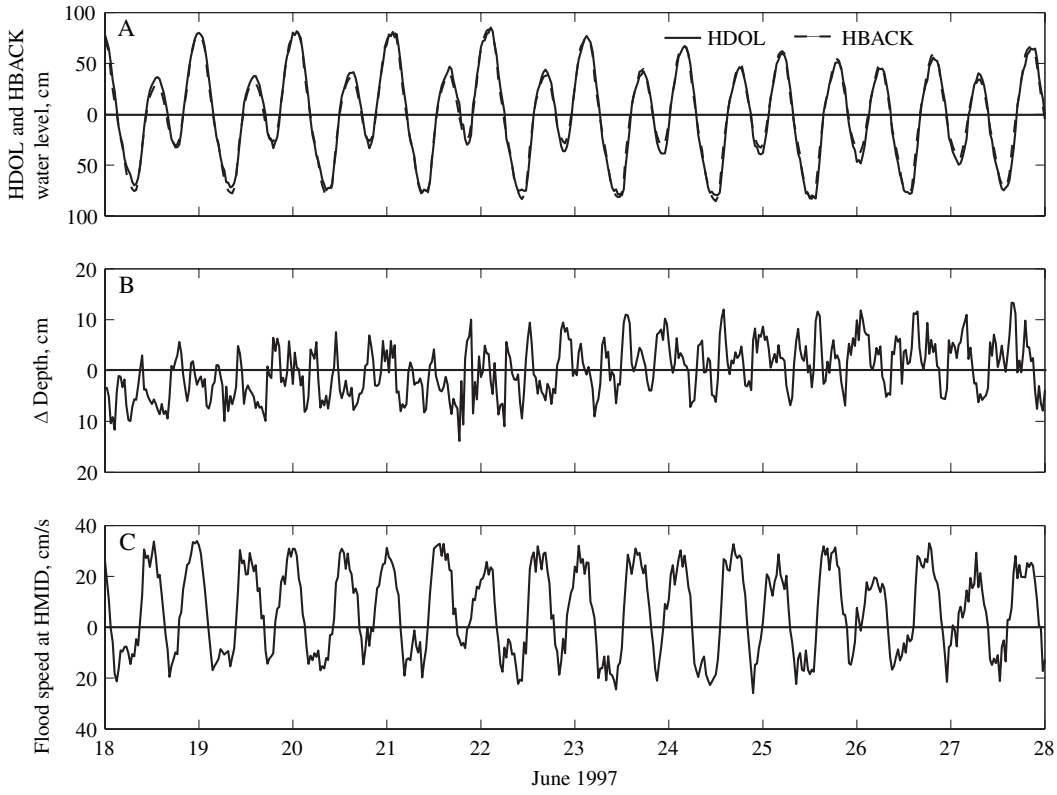

Fig. 7. Lack of floodtide pulses in Honker Bay. (A) Demeaned water level at sites HDOL and HBACK; (B) high frequency water surface difference between the mouth (HDOL) and back (HBACK) of Honker Bay; (C) flood speed at HMID.

φ is the porosity (volume of voids/total volume = 0.90) of the top bed layer, τ_{ce} is the critical shear stress for erosion ($=0.05\,\mathrm{N\,m^{-2}}$), and τ_b is the bed shear stress determined by the hydrodynamic routines. Underlying the entire hydrodynamic grid is a one-layer bed structure that interacts with the source/sink terms to maintain a mass balance in the domain. Thus the bed elevation changes caused by resuspension and deposition are simulated. For the simulations the bed thickness was initially set to 1.0 m thick of spatially uniform single grain size with sediment characteristics of a $0.5\,\mathrm{mm\,s^{-1}}$ settling velocity and density of $2650\,\mathrm{kg\,m^{-3}}$. Simulations were performed for a homogeneous system. Variations of density can greatly affect transport of suspended-sediment, however, this study is emphasizing floodtide pulses in a shallow (well-mixed) subembayment where the vertical density structure has minor influences on the transport processes. Simulations started with the domain at rest and continued for 10 days with a 30 s time step.

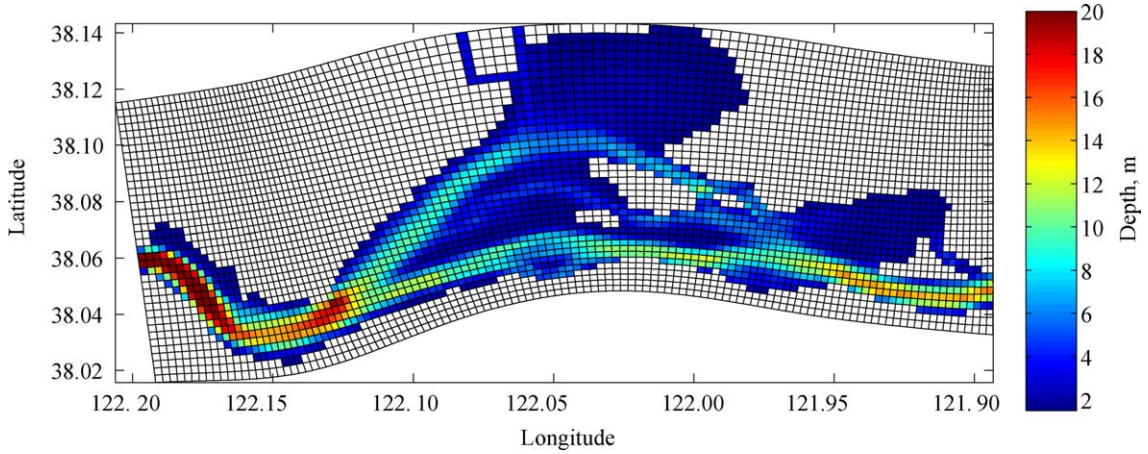

Fig. 8. Numerical grid and bathymetry of Suisun Bay including Grizzly and Honker Bays.

Table 3
Sea level tidal constituents used for western boundary of realistic bathymetry model (Warner et al., 1999)

Name	Cycles/day	Amplitude (cm)	Phase (κ')
O1	0.92954	17.5	126.00
K1	1.00274	40.7	151.20
M2	1.93227	65.1	4.00
S2	2.00000	8.20	49.00
N2	1.89598	8.00	2.89
M4	3.86455	1.6	302.00

3.2. Results

The numerical model results compare well with the field observations. A comparison of water level time series from the numerical simulation to the observed data at site GC (Fig. 9A) shows that the simulation is in phase with the observed data but does not fully respond to the observed semi-diurnal signal. This is most likely due to the boundary forcing and inclusion of additional harmonic terms would provide a greater fit to observations. The goal of this exercise is to determine if the numerical model can reproduce the observed process of the floodtide pulse and use the model to assess the significance and impact of the process on sediment dynamics of Grizzly Bay.

Despite the minor variation of observed to modeled tidal amplitudes, the modeled difference in sea level from the mouth of Grizzly Bay to the back (GRNC–GB) compares well with the observed difference (Fig. 9B). Estimates of maximum sea level difference by the numerical model are within a few centimeters of the observed data, and the numerical model captures the decrease in amplitude as the diurnal inequality diminishes. The velocity in the middle of the bay reproduces the floodtide pulse (Fig. 9C). However, the model overestimates the ebb current, perhaps due to local nonlinearities in the observational data not included in the model. The SSC in the numerical results at site GC shows maximum values immediately following the floodtide pulse (Fig. 9D), resulting from local resuspension and advection. The suspended-sediment flux (Fig. 9E, positive flood tide direction) is directed into Grizzly Bay, showing landward transport of sediment towards the back of the bay.

Contrastingly, the numerical simulations show no floodtide pulses in Honker Bay, consistent with the observational data. Time series of model sea level at sites HDOL and HBACK (Fig. 10A) are in phase with approximately the same amplitude, and the difference in sea level of these sites oscillates between ± 10 cm (Fig. 10B). However, the difference in sea level does not show a floodtide pulse at the lower low tides. Using the

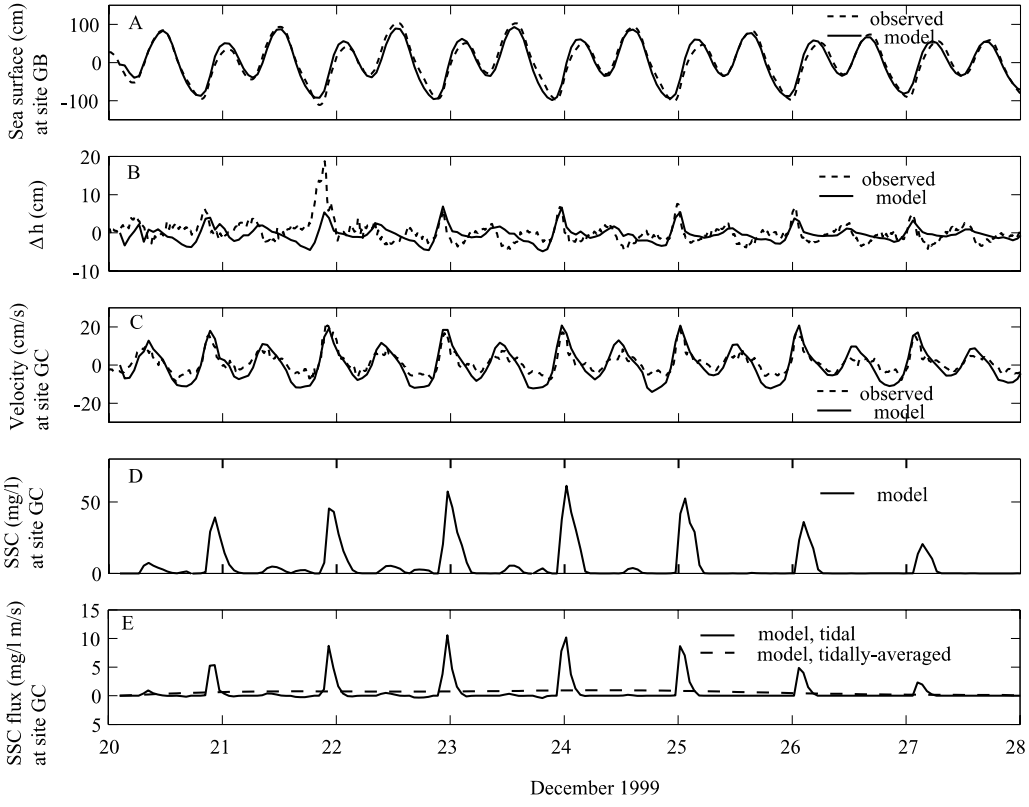

Fig. 9. Comparison of numerical simulations results to field observations for (A) sea level at site GC; (B) difference in water level from site GRNC to GB; (C) velocity at site GC; (D) SSC at site GC; (E) SSC flux at site GC.

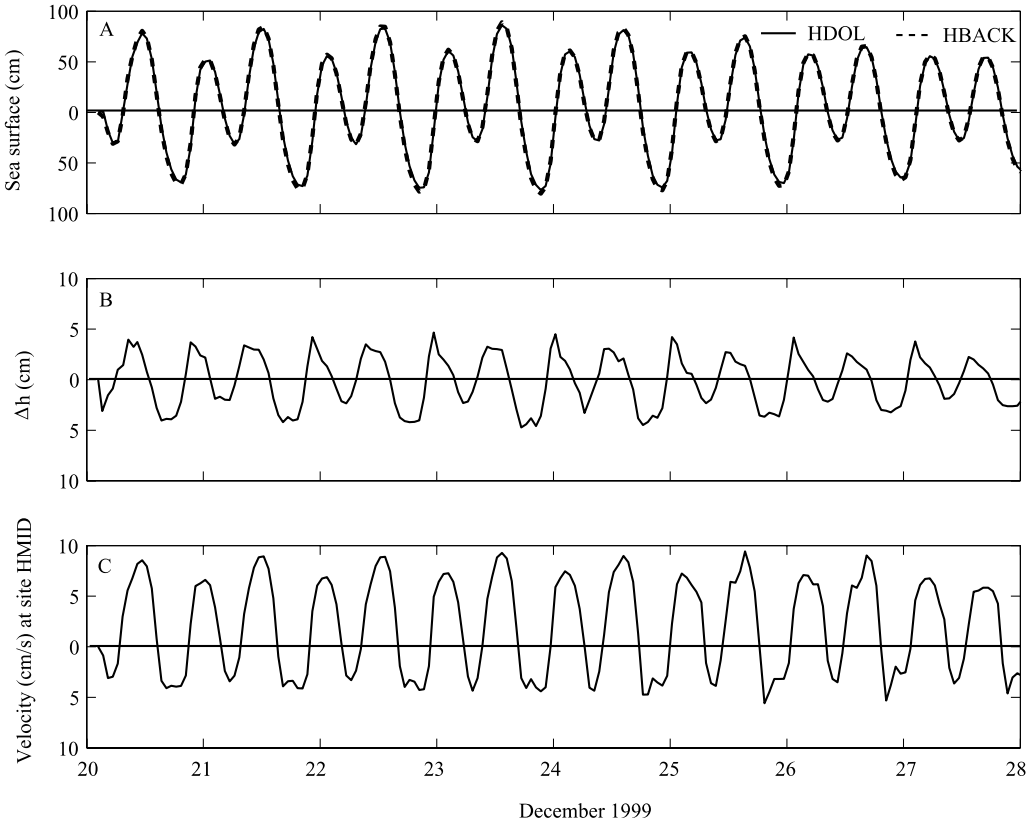

Fig. 10. Numerical simulation results for Honker Bay showing no floodtide pulse during the same time period as Fig. 7; (A) model water level at sites HDOL and HBACK; (B) difference in water level between sites HDOL and HBACK; (C) velocity in center of Honker Bay at site HMID.

distance between sites of approximately 4 km, yields a barotropic gradient ($\partial\eta/\partial x$) on the order of 2×10^{-5} m/m, a similar scaling as in Grizzly Bay. Fig. 10C shows the model velocity in the center of Honker Bay at site HMID, which also does not produce a floodtide pulse. The slightly greater water depths in Honker Bay (compared to Grizzly Bay) and possibly the geometric differences at the bay entrance are responsible for the lack of floodtide pulse generation.

4. Numerical simulation of an idealized bay–channel system

4.1. Methods

To examine the process of the floodtide pulse development, numerical simulations are conducted in an idealized model domain consisting of a straight rectangular channel with an adjacent side embayment. For a base (reference) simulation the channel is 25 000 m in length, 500 m in width, and 8 m deep (Fig. 11). The adjacent shallow embayment is centered on the north side of the channel and is 5 km^2. The model domain is discretized with a rectilinear finite difference grid of 100×55 cells resulting in x- and y-grid increments of 250 m and 100 m, respectively. A reference simulation held the mean bay depth (h_b) at 2.0 m and imposed a friction coefficient (C_d) of 0.002. Results from observational data identified that generation of the shallow water tides was necessary to produce the floodtide pulses. To investigate the importance of shallow tide generation, additional experiments were conducted to vary the relative depths of the bay to channel and to vary the magnitude of bottom friction. These comparison simulations were performed by holding C_d at the reference value and varying h_b with values of 1, 4 and 8 m; and holding h_b at the reference value and varying C_d with values of 0.001, 0.004, and 0.008.

For all the simulations, closed boundaries are assumed to be free slip walls. The free surface at the west end of the channel (η_{west}) is forced with a time varying displacement as the summation of a diurnal 24 h period (ω_1) and a semi-diurnal 12 h period (ω_2) as $\eta_{west} = -0.5\sin(\omega_1 t) - 0.8\sin(\omega_2 t)$. Radiation conditions are imposed on the eastern end of the channel and no river flow is stipulated. A constant temperature of 10 °C and constant salinity of 15 are specified.

The same numerical model ROMS is applied here as for the realistic bathymetric simulations with equivalent parameter values of an initial 1.0 m bed thickness of spatially uniform single grain size sediment, an erosion rate of 1×10^{-4} kg m^{-2} s^{-1}, a settling velocity of 0.5 mm s^{-1}, density of 2650 kg m^{-3}, and porosity of

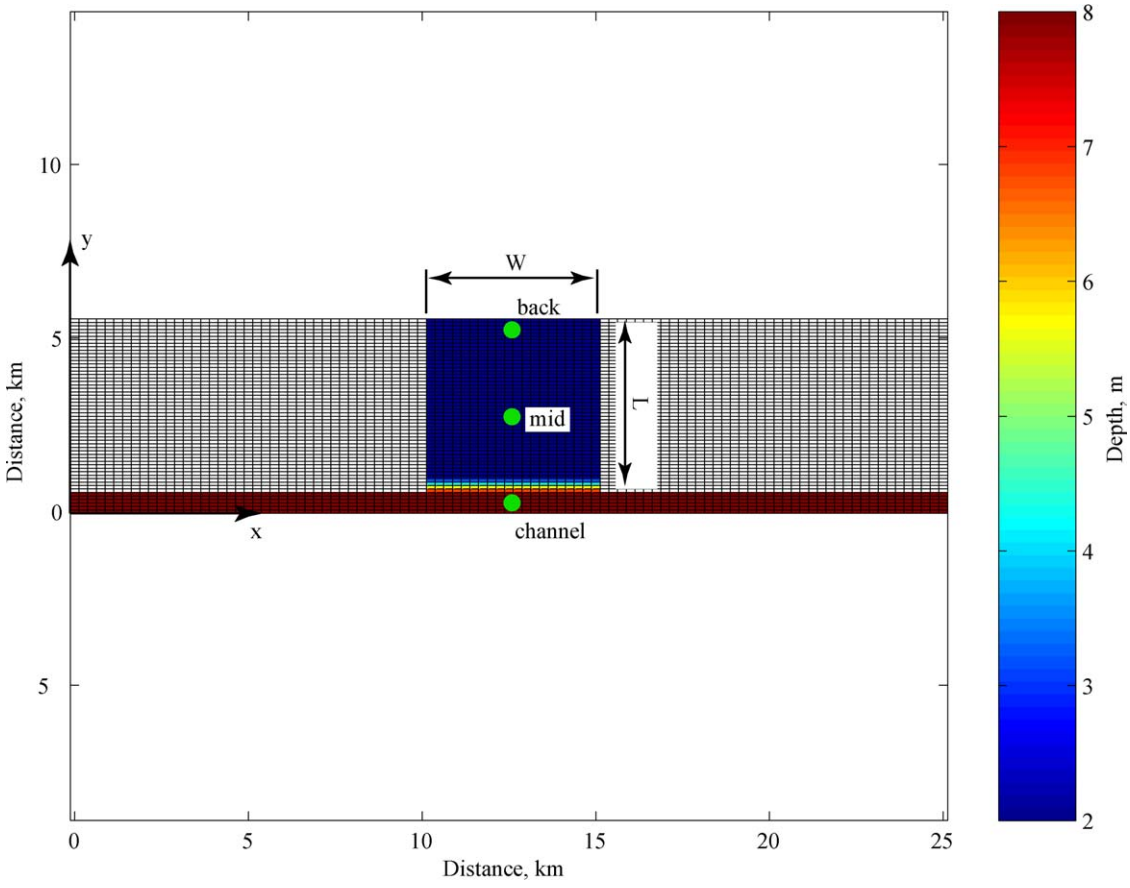

Fig. 11. Rectilinear grid for idealized bathymetric numerical experiments.

0.90. The model time step was 30 s and each simulation was run for five tidal cycles. After two tidal cycles the system developed a dynamic equilibrium and results will only be shown for the final three tidal cycles.

4.2. Results of reference simulation

The reference simulation results demonstrate differences between the response of the main channel and shallow subembayment to the tidal forcing. In the main channel the water level lags the depth-averaged along channel velocity component by approximately 1 h (Fig. 12) representative of a partially progressive wave. However, in the shallow side embayment the phase relation between velocity and sea level is more representative of a standing wave with slack water occurring near the peak water level displacements. Sea level displacements in the channel and side embayment are on the same order of magnitude but the velocity in the channel reaches a peak current of approximately 0.50 m/s but only reaches a peak current of approximately 0.15 m/s in the bay. This difference in velocity is due to the increased importance of friction in the shallow bay compared to the channel.

Simulated time series of sea level and velocity at locations in the channel (channel), middle of the bay (mid), and back of the bay (back), demonstrate the floodtide pulse (Fig. 13). Sites "channel" and "back" exhibit nearly identical sea level responses (Fig. 13A), however, there are small but significant differences in the phase and amplitudes of the tides. This difference is pronounced by observing the sea level gradient from "channel" to "back" (Fig. 13B). Typically the difference in sea level is on the order of ± 4 cm, however at the lower low tides a peak difference in sea level reaches a value of nearly 8 cm resulting in a barotropic gradient on the order of 2×10^{-5} m/m (near hours 6, 30, and 54). Maximum sea level gradients are coincident with maximum velocities. Floodtide spikes in velocity reach magnitudes of nearly 20 cm/s (Fig. 13C). The time series of SSC (Fig. 13D) however shows a maximum value slightly after the floodtide. The peak of SSC typically will lag the maximum velocity (and bottom stress) because the suspended-sediment is a summation of erosive and depositional fluxes. The upward movement of sediment continues to dominate the process until a short time after the maximum bottom stress resulting in the peak of sediment lagging the maximum velocity. Additionally, local advection processes and any spatial

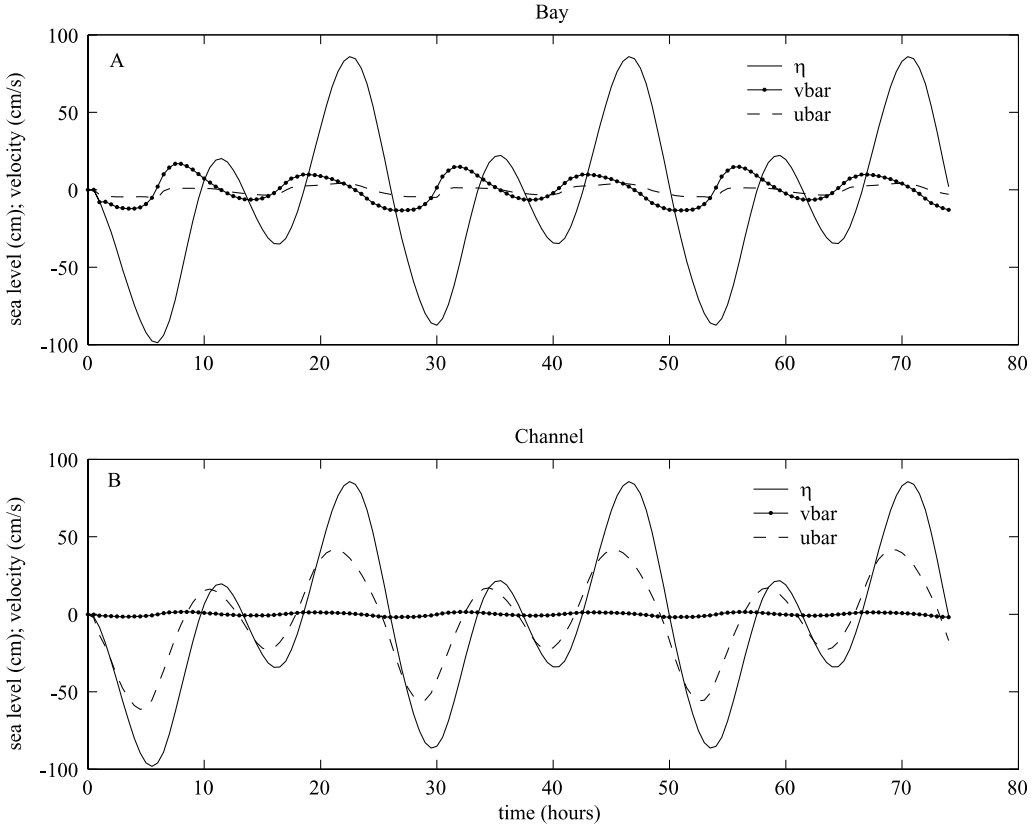

Fig. 12. Comparison of sea level (η), depth-averaged longitudinal (x-direction) velocity component (*ubar*), and lateral (y-direction) velocity component (*vbar*) in (A) the shallow bay vs. (B) the deep tidal channel.

differences in local resuspension can shift the phase of the SSC time series. At the occurrence of the pulse, there is a decrease in the bed elevation and at the end of the flood tide the greatest increase in the bed elevation occurs (Fig. 13E). This process creates a suspended-sediment flux into the bay as shown in Fig. 13F. On the tidal time scale the sediment flux magnitude ($|\text{vbar} * \text{SSC}|$) is greatest during the flood tide pulse. On the tidally averaged time scale (low pass filtered with 40 h cutoff period) the suspended-sediment flux is into the bay.

4.3. Results of variations to reference simulation

As identified in Eqs. (1)–(3), the ratio of free surface displacement to mean depth (η/h) and the magnitude of the bottom drag coefficient (C_d) are two parameters responsible for generation of tidal asymmetries, which in turn generate floodtide pulses. Additional numerical experiments were performed to identify the importance of bay/channel depth ratio (η_b/h_b) and magnitude of C_d on the generation of the nonlinear shallow water tides and hence floodtide pulses. Numerical experiments varied the bay depth (h_b) and friction coefficient and the results are summarized in Fig. 14. The left vertical axes of panels A–C scale the tidal amplitude ($\eta_b = 0.8$ m) relative to bay depth ($h_b = 1$, 2, 4, and 8 m) while holding $C_d = 0.002$. The right vertical axes are variations of drag coefficient ($C_d = 0.001$, 0.002, 0.004, and 0.008) while holding $h_b = 2$ m.

Fig. 14A plots the η_b/h_b ratio and C_d magnitude vs. wave celerity in the bay, calculated from the propagation speed of the S2 tide relative to the base simulation. The smallest η_b/h_b ratio (largest value of h_b) equates the bay depth and channel depths and results in very large wave celerity, emphasizing that the bay may be acting in resonance. As the η_b/h_b ratio increases the wave celerity reduces dramatically. Increases in C_d also reduce the wave celerity. These processes demonstrate the first order effect of friction—to reduce the propagation speed of the tide and delay the timing of high and low waters.

Fig. 14B displays the generation of overtides by plotting the ratio of S4/S2 amplitudes at a mid bay location. As the η_b/h_b ratio increases the generation of shallow water overtides greatly increases. Increases in the drag coefficient only slightly increase the generation of nonlinear tides. This process (in part) can be explained by the friction term $C_d(\bar{u}|V|/h+\eta)$ from Eq. (2). As the magnitude of η/h approaches unity, the denominator will be significantly smaller at low tide and larger at high tide. This generates an asymmetric response of increased frictional loss at low tide and

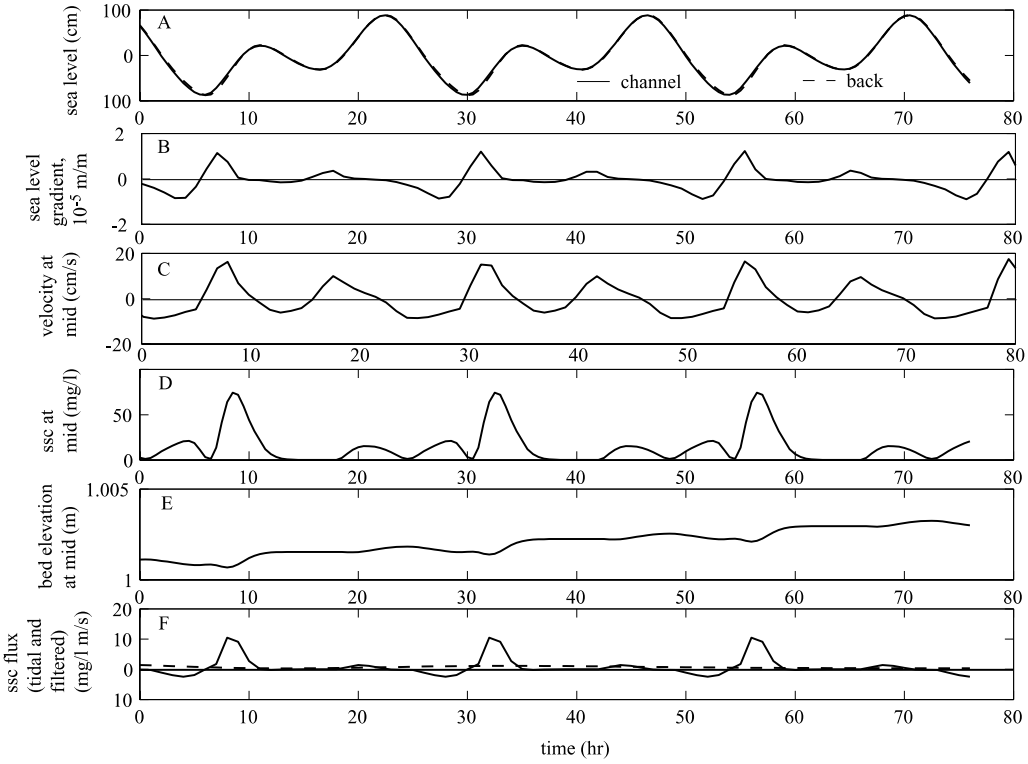

Fig. 13. Time series of (A) sea level at channel and back; (B) sea level difference from channel-back; (C) velocity at mid; (D) SSC at mid; (E) bed elevation at mid; (F) tidal and tidally averaged suspended-sediment flux.

decreased loss at high tide, skewing the tidal form with low tide occurring later and high tide earlier. Subtraction of this asymmetric shape from the original tide results in the development of overtides. Variations of C_d cannot directly generate nonlinear tides but this factor slows the propagation speed and indirectly (through continuity) can generate nonlinear tides. Therefore the generation of overtides is dominated by relative changes in depth rather than changes in friction coefficient.

Fig. 14C demonstrates the significance of h_b and C_d to the barotropic gradient between the channel and bay. As the η_b/h_b ratio increases the barotropic gradient increases. This is due to the increase in amplitude of the nonlinear tides that increases the magnitude of the floodtide pulse. As demonstrated in Fig. 4, the nonlinear (shallow water) tides are necessary to develop the floodtide pulses. Increases in C_d also increase the barotropic gradients caused primarily by the reduction in wave celerity.

Fig. 14D compiles the results from panels A–C and relates the relative wave celerity (solid line) and relative amplitude of nonlinear tides (dashed line) to the barotropic gradient. The relative wave celerity displays a relationship that is inversely proportional to the barotropic gradient. Filled circles denote experiments with constant C_d and variation of η_b/h_b and bold plus signs denote experiments with variation of C_d and constant η_b/h_b. To develop a large barotropic gradient, the relative wave celerity needs to be very small, consistent with large η_b/h_b ratios from experiments with very shallow depths. As the depth of the bay increases, the relative wave celerity increases and the magnitude of the barotropic gradient decreases. From Fig. 14D, to produce a strong barotropic gradient ($\sim 10^{-5}$ m/m) requires relative wave celerities less than ~ 1 which relates to $\eta_b/h_b > \sim 0.5$. Variations of η_b/h_b (filled circles) are more important in generation of strong barotropic gradients than changes in the bottom friction (bold plus signs).

Fig. 14D also displays the generation of overtides by plotting the ratio of S4/S2 amplitudes. Open circles denote experiments with constant C_d and variation of η_b/h_b and plus signs denote experiments with variation of C_d and constant η_b/h_b. Increases in generation of tidal asymmetry denoted by increases in S4/S2 ratio produce almost a linear increase in the strength of the barotropic gradient. From Fig. 14D, to produce a strong barotropic gradient ($> 10^{-5}$ m/m) requires relative S4/S2 amplitudes $> \sim 0.075$ which again relates to $\eta_b/h_b > \sim 0.5$. Variations of η_b/h_b (open circles) are more important in generation of strong barotropic gradients than changes in the bottom friction (plus signs).

5. Conclusions

In shallow waters, surface gravity waves (tides) propagate with a speed proportional to the square root

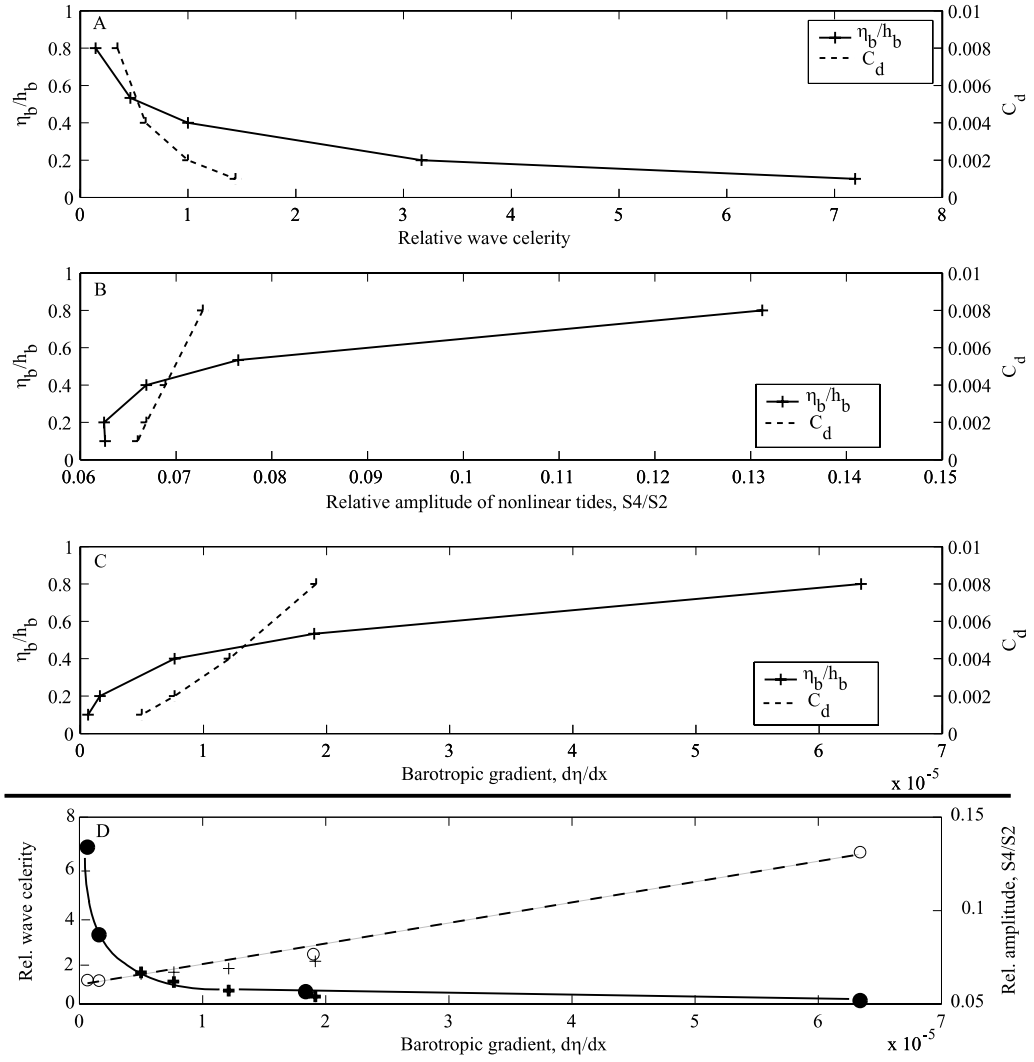

Fig. 14. Affects of η_b/h_b and C_d on (A) relative wave celerity in the bay; (B) generation of nonlinear tides in the bay; and (C) barotropic gradient between channel and bay. (D) Summarizes results from (A), (B), and (C) to relate relative wave celerity and relative amplitude of nonlinear tides to the barotropic gradient.

of the total water depth. In a shallow bay where $\eta/h \sim 1$, the tide will propagate faster at high tide than at low tide, increasing the importance of friction, nonlinear continuity and momentum terms. The increased importance of the nonlinear terms generates tidal asymmetries. At locations where a deep tidal channel borders a shallow embayment stronger tidal asymmetries will be generated in the shallow bay compared to the deeper channel. These tidal asymmetries can create barotropic gradients between the bay and channel, producing strong velocity spikes we term floodtide pulses that promote bayward flux of suspend sediment.

In Grizzly Bay (part of northern San Francisco Bay, USA), field observations verified the occurrence of floodtide pulses during the lowest low tides of the year. No pulses were observed in neighboring Honker Bay, which has an average depth 32 cm greater than Grizzly Bay. A numerical model using realistic bathymetry of northern San Francisco Bay simulated the floodtide pulse in Grizzly Bay but not in Honker Bay, consistent with the observational data. Model results also demonstrated that floodtide pulses in Grizzly Bay transported sediment into the subembayment, creating a landward flux of material. These results demonstrate that bathymetry is an important factor in determining the occurrence and magnitude of floodtide pulses in shallow subembayments adjacent to deep channels. The lack of observed flood tide pulse in Honker Bay may be caused by the slightly higher mean water depths, but may also be due to the more constricting sill at the bay mouth.

Numerical simulations of an idealized bay–channel system identify the development of a floodtide pulse that becomes more significant as the depth of the embayment decreases (increase of η_b/h_b). Decreases in bay depth dramatically increase the generation of nonlinear tides, enhancing the development on strong barotropic

gradients between the bay and channel. Increases to the friction coefficient produce a first order friction response of decreasing the wave celerity, delaying the timing of high and low tides and thus generating slightly increased barotropic gradients between the bay and channel. To produce a strong barotropic gradient ($>10^{-5}$ m/m) requires $\eta_b/h_b > \sim 0.5$. Variations of η_b/h_b are more important in generation of strong barotropic gradients than changes in the bottom friction.

Acknowledgements

We gratefully acknowledge support from the USGS Priority Ecosystem Studies Program and the USGS Mendenhall Post-Doctoral Research Program for support of John C. Warner. We thank the developers of ROMS for the open access to their code, Jessie Lacy for her review and sharing her knowledge of Honker Bay with us, Neil Ganju for his review of the manuscript, and Greg Brewster, Curt Battenfeld, Paul Buchanan, Jay Cuetara, Jim George, Rob Sheipline, Brad Sullivan, and Jon Yokomizo for their help in collecting field data in Suisun Bay.

References

Ariathurai, C.R., Arulanandan, K., 1978. Erosion rates of cohesive soils. Journal of Hydraulics Division, ASCE 104 (2), 279–282.

Aubrey, D.G., Speer, P.E., 1985. A study of the non-linear propagation in shallow inlet/estuarine systems Part I: observations. Estuarine, Coastal and Shelf Science 21, 185–205.

Chassignet, E.P., Arango, H.G., Dietrich, D., Ezer, T., Ghil, M., Haidvogel, D.B., Ma, C.-C., Mehra, A., Paiva, A.M., Sirkes, Z., 2000. DAMEE-NAB: the base experiments. Dynamics of Atmospheres and Oceans 32, 155–183.

Conomos, T.J., Smith, R.E., Gartner, J.W., 1985. Environmental setting of San Francisco Bay. In: Cloern, J.E., Nichols, F.H. (Eds.), Temporal Dynamics of an Estuary: San Francisco Bay. Dr. W. Junk Publishers, Kluwer Academic, pp. 1–12.

Conover, W.J., 1980. Practical Nonparametric Statistics, second ed. John Wiley & Sons, 493 pp.

Ezer, T., Arango, H.G., Shchepetkin, A.F., 2002. Developments in terrain-following ocean models: intercomparisons of numerical aspects. Ocean Modelling 4, 249–267.

Friedrichs, Carl T., Lynch, D.R., Aubrey, D.G., 1992. Velocity asymmetries in frictionally-dominated tidal embayments: longitudinal and lateral variability. In: David, Prandle (Ed.), Dynamics and Exchanges in Estuaries and the Coastal Zone. American Geophysical Union, Washington, D.C., pp. 277–312 (Chapter 15).

Haidvogel, D.B., Arango, H.G., Hedstrom, K., Beckmann, A., Malanotte-Rizzoli, P., Shchepetkin, A.F., 2000. Model evaluation experiments in the north Atlantic Basin: simulations in nonlinear terrain-following coordinates. Dynamics of Atmospheres and Oceans 32, 239–281.

Helsel, D.R., Hirsch, R.M., 1992. Statistical Methods in Water Resources: Studies in Environmental Science, 49. Elsevier, 522 pp.

Krone, R.B., 1979. Sedimentation in the San Francisco Bay system. In: Conomos, T.J. (Ed.), San Francisco Bay, the Urbanized Estuary. Pacific Division of the American Association for the Advancement of Science, San Francisco, pp. 347–385.

Lacy, J.R., 2000. Circulation and transport in a semi-enclosed estuarine subembayment. Ph.D. Dissertation, Department of Civil and Environmental Engineering, Stanford University, Stanford, CA.

Li, C., O'Donnell, J., 1997. Tidally driven residual circulation in shallow estuaries with lateral depth variation. Journal of Geophysical Research 102 (C13), 27915–27929.

Parker, B.B., 1991. The relative importance of the various nonlinear mechanisms in a wide range of tidal interactions (review), Paper 13. In: Bruce, Parker (Ed.), Tidal Hydrodynamics. National Ocean Service, National Oceanic and Atmospheric Administration, pp. 237–269.

Ruhl, C.A., Schoellhamer, D.H., 1999. Time series of suspended-solids concentration in Honker Bay during water year 1997, Regional Monitoring Program 1997 Annual Report.

Ruhl, C.A., Schoellhamer, D.H. Spatial and temporal variability of suspended-sediment concentrations in a shallow estuarine environment. San Francisco Estuary and Watershed Science, in press.

Ruhl, C.A., Schoellhamer, D.H., Stumpf, R.P., Lindsay, C.L., 2001. Combined use of remote sensing and continuous monitoring to analyse the variability of suspended-sediment concentrations in San Francisco Bay, California. Estuarine, Coastal and Shelf Science 53, 801–812.

Shchepetkin, A.F., McWilliams, J.C. The Regional Ocean Modeling System: a split-explicit, free-surface, topography-following coordinates ocean model. Draft at http://marine.rutgers.edu/po/index.php, in press.

Schuepfer, F.E., Apicella, G.A., DeSantis, V.J., 1995. Significance of lateral elevation gradients in tidally affected tributaries. In: Spaulding, Cheng (Eds.), ASCE Estuarine and Coastal Modeling. Proceedings of the 4th International Conference, October 26–28.

Speer, P.E., Aubrey, D.G., 1985. A study of the non-linear propagation in shallow inlet/estuarine systems Part II: Theory. Estuarine, Coastal and Shelf Science 21, 207–224.

Umlauf, L., Burchard, H., Hutter, K., 2003. Extending the k–w turbulence model towards oceanic applications. Ocean Modelling 5, 195–218.

Valle-Levinson, A., O'Donnell, J., 1996. Tidal interaction with buoyancy-driven flow in a coastal plain estuary. In: Aubrey, David G., Friedrichs, Carl T. (Eds.), Buoyancy Effects on Coastal and Estuarine Dynamics. Coastal and Estuarine Studies, 53, American Geophysical Union. Washington, D.C., pp. 265–281.

Warner, J.C., Schladow, S.G., Schoellhamer, D.H., 1999. Summary and analysis hydrodynamics and water-quality data for the Napa/Sonoma Marsh Complex, Final Report, Equipment Deployment from September 1997 to March 1998. University of California, Davis, Environmental Dynamics Laboratory Report No. 98–07, 114 pp.

Warner, J.C., Sherwood, C.R., Arango, H.G., Signell, R.P. Performance of four turbulence closure models implemented using a generic length scale method. Ocean Modelling, in press.

Wilcox, D.C., 1988. Reassessment of the scale determining equation for advance turbulence models. AIAA Journal 26 (11), 1299–1310.